# Supplemental Material: "Absolutely Stable Spatiotemporal Order in Noisy Quantum Systems"

Max McGinley, Sthitadhi Roy, and S. A. Parameswaran

### Continuum time limit

In this section, we discuss in detail the continuum-time limit described in the main text, and compare this to the time-dependent Lindblad dynamics studied in Ref. [34].

The correction step $\mathcal{N}_2$ involves projective measurements, which are intrinsically discontinuous events. Nevertheless, a continuum time limit can be taken by applying the three-qubit correction processes $\mathcal{N}_{\mathrm{T},j}$ [Eq. (2)] according to independent random Poisson processes for each $j$, with some correction rate $\Gamma$. Specifically, in an infinitesimal time window $\mathrm{d}t$, the channel $\mathcal{N}_{\mathrm{T},j}$ is applied with probability $\Gamma \mathrm{d}t$ for each $j$, and we do nothing otherwise (with probability $1 - N\Gamma \mathrm{d}t$). Since the Poisson processes are uncorrelated in time, the resulting dynamics can be described by a Markovian Lindblad master equation $\mathrm{d}\rho/\mathrm{d}t = \mathcal{L}[\rho]$ with time-independent superoperator $\mathcal{L}$, which without loss of generality can be cast in the standard diagonal form [60]

$$\mathcal{L}[\rho] = -\mathrm{i}[H, \rho] + \sum_{\mu} L_\mu \rho L_\mu^\dagger - \frac{1}{2}\{L_\mu^\dagger L_\mu, \rho\}, \tag{S1}$$

The operators $\{L_\mu\}$ are referred to as jump operators, and $H$ is Hermitian, playing the role of an effective Hamiltonian.

Evidently, the Lindbladian $\mathcal{L}$ pertaining to the stochastic dynamics described above is given by

$$\mathcal{L} = \lim_{\substack{p,\mathrm{d}t\to 0 \\ p=\Gamma \mathrm{d}t}} \frac{(1-Np)\mathrm{id} + p\sum_j \mathcal{N}_{\mathrm{T},j}}{\mathrm{d}t} \tag{S2}$$

where id is the identity superoperator. Using this expression, one can readily determine that $H = 0$, and that there are four jump operators $\{L_{j,m} : m = 1, 2, 3, 4\}$ associated with each site $j$

$$L_{j,m} = \sum_{b=\pm} L_{j,m,b} \tag{S3}$$

$$L_{j,1,b} = \sqrt{\Gamma}\, |b_j b_{j+\hat{e}} b_{j+\hat{n}}\rangle \langle b_j b_{j+\hat{e}} b_{j+\hat{n}}| \tag{S3a}$$

$$L_{j,2,b} = \sqrt{\Gamma}\, |b_j \bar{b}_{j+\hat{e}} b_{j+\hat{n}}\rangle \langle b_j \bar{b}_{j+\hat{e}} b_{j+\hat{n}}| \tag{S3b}$$

$$L_{j,3,b} = \sqrt{\Gamma}\, |b_j b_{j+\hat{e}} \bar{b}_{j+\hat{n}}\rangle \langle b_j b_{j+\hat{e}} \bar{b}_{j+\hat{n}}| \tag{S3c}$$

$$L_{j,4,b} = \sqrt{\Gamma}\, |b_j b_{j+\hat{e}} b_{j+\hat{n}}\rangle \langle b_j \bar{b}_{j+\hat{e}} \bar{b}_{j+\hat{n}}| \tag{S3d}$$

where $|b_j b_{j+\hat{e}} \cdots\rangle$ is shorthand for $(|0\rangle_j + b_j |1\rangle_j)/\sqrt{2} \otimes (|0\rangle_{j+\hat{e}} + b_j |1\rangle_{j+\hat{e}})/\sqrt{2} \otimes \cdots$; we write $\bar{b}$ to denote $-b$; and as usual $j + \hat{e}$, $j + \hat{n}$ are the Eastern and Northern neighbours of qubit $j$. Each of the four jump operators comes from a particular term in the sum in Eq. (2), which correspond to the different outcomes that could occur when measuring both domain wall operators. The Lindbladian can be supplemented with a (possibly time-dependent) Hamiltonian to describe a driving field that effects the oscillation of magnetization (in place of the discrete pulse channel $\mathcal{N}_1$), as well as additional jump operators that model unintended dissipative effects.

Now that the dynamics is cast in a Lindblad form, it is possible to compare directly with that of Ref. [34]. There, the jump operators act on a given spin $j$ and its four North, East, South, and West neighbours. Each jump operator has the form

$$L_{j,\vec{b}} = \sqrt{\Gamma}\, |f(\vec{b})_j b^{(e)}_{j+\hat{e}} b^{(n)}_{j+\hat{n}} b^{(w)}_{j+\hat{w}} b^{(s)}_{j+\hat{s}}\rangle \langle b^{(c)}_j b^{(e)}_{j+\hat{e}} b^{(n)}_{j+\hat{n}} b^{(w)}_{j+\hat{w}} b^{(s)}_{j+\hat{s}}| \tag{S4}$$

where $\vec{b}$ is a five-dimensional vector whose components $\{b^{(c)}, b^{(e)}, b^{(n)}, b^{(w)}, b^{(s)}\}$ are 0 or 1. The function $f : \{0,1\}^{\times 5} \to \{0,1\}$ implements a majority vote of the 5 constituent spins.

The dynamics described above differs from ours in two important ways. Firstly, the jump operator (S4) updates the central spin depending on the majority of itself and its four neighbours, whereas in our case [Eq. (S3)] only the Northern and Eastern neighbours affect the flip process. In essence, the isotropic majority vote rule induces local transitions according to whether or not they reduce the energy of the system with respect to the Ising Hamiltonian $H_{\mathrm{Ising}} = \sum_{\langle j,j'\rangle} X_j X_{j'}$; thus if no other terms are added the dynamics will obey detailed balance with respect to $H_{\mathrm{Ising}}$. In contrast, the jump operators (S3) found in our model do not satisfy detailed balance, since the interactions between neighbouring spins are strictly one-way ($j$ will flip depending on the state of $j + \hat{n}$, but the probability of $j+\hat{n}$ flipping is independent of the state of $j$). The intrinsically non-equilibrium nature of the NEC-based dynamics allows for truly robust bistability, whereas the equilibrium model can only exhibit bistability in regions of parameter space of measure zero – specifically on subspaces where Ising symmetry is respected. (For a detailed discussion of the differences between classical automata based on reversible vs. irreversible update rules, see e.g. Refs. [48, 61].)

Although the stabilization terms in Ref. [34] obey detailed balance, it is still possible to reach a bistable region if additional driving is added, e.g. using a time-dependent

Hamiltonian, which takes the system away from equilibrium. Indeed, one can argue that the majority vote jump operators *can* stabilize a period-2 time-crystalline phase against symmetry-breaking perturbations: The effect of any bias favouring $+X$ magnetization over $-X$ (e.g. a jump operator $L_{j,\text{bias}} = |+\rangle\langle -|_j$) acting over one time period will be cancelled out by itself during the next time period, since the sign of the magnetization is reversed each step [49]. Thus, we expect that the phase diagram of the model of Ref. [34] will feature a robust DTC phase, but the ferromagnetic phase that we found in our model will not be present, since any bias will not be cancelled out and will amplify over time. Moreover, the same strategy will not be able to stabilize a time crystal with period $n > 2$, whereas our NEC-model could in principle be generalized to realise higher-period time crystals.

The second key difference between the two models is that the jump operators (S4) are fully incoherent: Any jump event fully collapses the wavefunction of the five constituent spins to a product of $\pm X_j$ eigenstates. In contrast, as discussed in the main text, coherences in the $X_j$ basis are partially preserved under our update rule. This can be seen immediately from the form of the jump operators (S3), each of which is a coherent sum of two operators that have identical domain wall configurations, but opposite magnetizations of each spin. An incoherent version of our rule could be devised where one would include each $L_{j,m,b}$ as a separate jump operator. Such a Lindbladian would differ from our model in that cross-terms such as $L_{j,m,+}\rho L^\dagger_{j,m,-}$ would not be present. Because of these cross-terms, any state within the Bloch sphere (coherent superpositions or classical mixtures) spanned by $|+^{\otimes N}\rangle$, $|-^{\otimes N}\rangle$ will be steady states of the coherent Lindbladian, whereas only classical mixtures are stabilized by the incoherent Lindbladian.

### NEC rule with open boundary conditions

In this section, we explain how to implement the NEC rule in an in-plane superconducting quantum processor without relying on periodic boundary conditions, which are not generally possible in experimental platforms. In brief, our strategy is to consider a NEC automaton on a torus embedded in 3-dimensional (3D) space (equivalent to a 2D system with periodic boundary conditions). We then 'flatten' the system in one of the three-dimensional directions to obtain a quasi-2D system with top and bottom layers. These two layers are then merged into one, which results in a truly 2D system with an annular shape. This system inherits the robust non-ergodic properties of the NEC rule without requiring any cross-wiring, thus allowing for on-chip realizations.

In describing this construction in detail, we find it instructive to work backwards, starting from the strictly 2D open-boundary geometry and showing that its dynamics mimics that of a system with periodic boundaries. The layout and connectivity of the physical qubits (both system and ancilla) are illustrated in Fig. S1(a). Each qubit is capacitively coupled to 6 neighbouring qubits in a triangular lattice structure. One-third of the qubits are ancillas, and the remaining two-thirds are split into two separate 'system' sublattices, drawn in red and green, respectively.

Within each system sublattice, we must determine which domain wall operators $W_{jj'} = X_j X_{j'}$ can be projectively measured, using the technique described in the main text. This requires $j$ and $j'$ to be both connected to at least one ancilla qubit in common. The pattern of effective connectivities defined by this condition is illustrated in Fig. S1(b) – each sublattice now forms a smaller triangular lattice, with open boundary conditions in the radial direction and periodic boundary conditions in the azimuthal direction. At this point, we can 'stitch together' the two sublattices at the inner and outer boundaries by adding connections between red and green qubits (these still satisfy the measurable domain wall criterion). We can then consider one sublattice (say red) to be the upper half of a torus, and the other to be the lower half. Specifically, in the standard two-angle parametrization of the torus $(\varphi, \theta)$, the red qubits reside on the region of poloidal angle $\theta \in [0, \pi)$, while the green qubits are mapped to $\theta \in [\pi, 2\pi)$.

This demonstrates that the 2D geometry in Fig. S1(a) can mimic that of a triangular lattice on a torus. We now need to generalize the quantum NEC measurement-feedback rule, which is defined for the square lattice. This problem has been solved in Ref. [62] for a broad class of (not necessarily regular) lattices with periodic boundary conditions. The 'sweep rule' introduced there specifies an update rule for classical spins that, like the NEC rule, depends only on the presence or absence of domain walls on particular bonds, and gives rise to provably robust bistability. One must pick a sweep direction $\vec{h}$, which determines the way in which regions of errors shrink. In our case, it is convenient to pick this to be along the toroidal direction $\hat{e}_\varphi$, i.e. the direction that corresponds to the polar coordinate of the annulus. With this choice, the sweep rule takes a particularly simple form, where one ignores two out of six of the connections emanating from each qubit, such that the remaining connections form a square lattice [see Fig. S1(c)], and the NEC rule can be applied as usual. However, other choices will also be possible, provided that they are consistent with the requirements of the sweep rule. As before, the resulting classical automaton can be used to define a quantum measurement-feedback loop that inherits the same error-correcting properties.

Since the sweep direction $\vec{h}$ winds around the toroidal direction, it is not possible to 'fill in' the hole at the centre of the annulus without encountering a point where

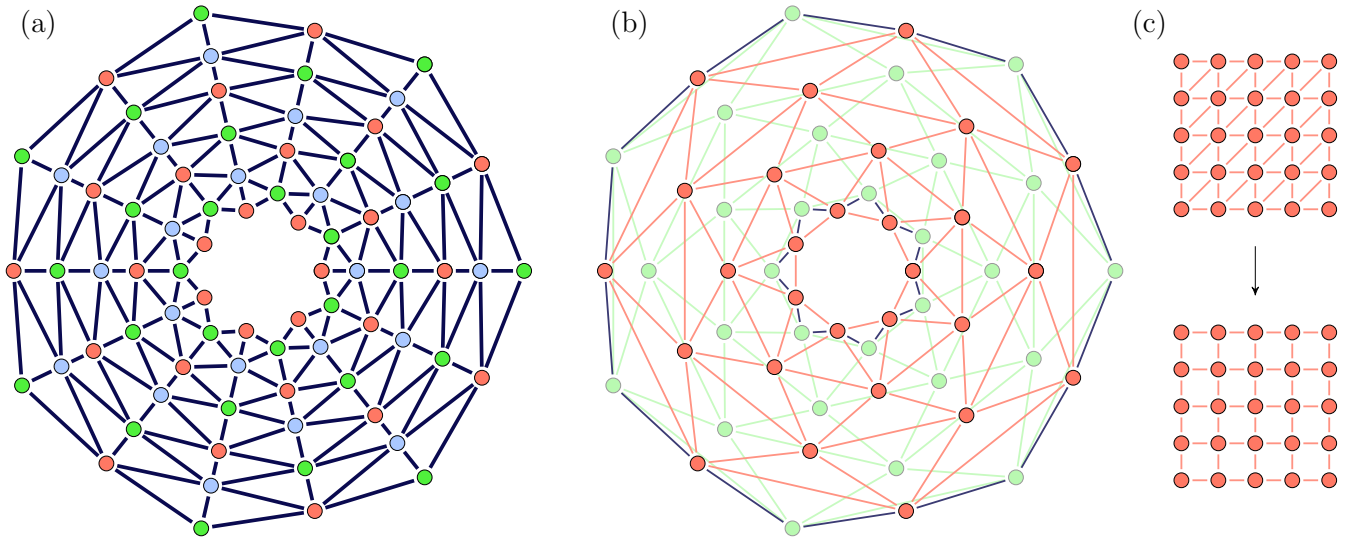


FIG. S1. (a) Layout and connectivity of physical and ancilla qubits in a 2D annular geometry that can emulate a system with periodic boundaries. As in Fig. 2, blue circles are ancilla qubits, and dark blue lines represent capacitive couplings. The physical qubits are divided into two sublattices, coloured in red and green. Altogether, the qubits form a triangular lattice where one direction (radial) has open boundaries, and the other (polar) is effectively periodic (b) Effective connectivity of the system qubits. The qubits are drawn in the same positions, with ancillas removed. Any two physical qubits connected by a line have the property that there exists at least one ancilla qubit to which both are directly coupled, so that a domain wall operator between the two physical qubits can be measured (see main text). The red and green sublattices each form a triangular lattice. (The green sublattice is drawn faintly to aid the eye.) At the inner and outer boundaries of the annulus, the two sublattices are joined together (dark blue lines), such that the radial direction becomes effectively periodic. (c) A square lattice (bottom) can be obtained from a triangular lattice (top, rotated 45° and stretched) by removing two out of six of the bonds coming out of each qubit.

the sweep direction has singular behaviour, which would cause the correcting mechanism to fail. If one wishes to have a simply connected 2D geometry, then one can repeat the trick of 'squishing' the periodic direction into two copies of an open direction. The result would be a 2D system with four sublattices, each of which map onto one of the four quadrants of the torus ($(\varphi,\theta) \in [n\pi,(n+1)\pi) \times [m\pi,(m+1)\pi)$, for $n,m = 0,1$). To do so will likely require higher connectivity of physical qubits, which may be challenging.

The annular embedding of the triangular lattice means that the distance between connected qubits grows as one moves away from the centre. Therefore, to make this design scalable with a fixed maximum qubit-qubit coupling distance, it may be necessary to insert extra qubits, forming disclinations of the triangular lattice. Since the sweep rule can be defined for lattices with such irregularities [62], it will still be possible to devise a measurement-feedback protocol with the same robust properties.

One unusual artefact of the setup we have proposed is that any correlated two-qubit errors that act on pairs of system qubits on opposite sublattices will look highly non-local under the toric mapping. Fortunately, the measurement-feedback protocol remains robust against these kind of errors. We have simulated the 2D annular system, including unitary errors that act on any pairs of qubits that are physically connected, regardless of which sublattice they are on. We have confirmed that the characteristic exponential scaling of the correlation time is still seen.

### Experimental domain wall measurement protocol

Here we demonstrate explicitly that the protocol for measuring domain wall operators described in the main text does indeed project the state of the system onto one of the eigenspaces of $W_{j,j'}$. We assume that the two system qubits involved $j$, $j'$ begin in an arbitrary pure state $|\psi\rangle_{jj'}$, and the ancilla $b$ begins in the state $|+\rangle_b = (|0\rangle_b + |1\rangle_b)/\sqrt{2}$. The gate $U_{\mathrm{CR},j,b,\pi/2} = e^{-\mathrm{i}\pi X_j Z_b/4}$ is applied, followed by $U_{\mathrm{CR},j',b,\pi/2}$. The resulting state is then

$$\begin{aligned}|\Phi\rangle &= e^{-\mathrm{i}\pi(X_j+X_{j'})Z_b/4}\,|\psi\rangle_{jj'} \otimes |+\rangle_b \\ &= \Big[\Pi_{X_j+X_{j'}=+2}(-\mathrm{i}Z_b) + \Pi_{X_j+X_{j'}=0} \\ &+ \ \Pi_{X_j+X_{j'}=-2}(+\mathrm{i}Z_b)\Big]\,|\psi\rangle_{jj'} \otimes |+\rangle_b\,, \end{aligned} \tag{S5}$$

where in the last equality we have decomposed the unitary operator as the direct sum of its action on the different eigenspaces of the operator $(X_j + X_{j'})$, spanned by

the projectors $\Pi_{X_j+X_{j'}} = \lambda$, for $\lambda = -2, 0, 2$. We have $Z_b |+\rangle_b = |-\rangle$, and also note that $\Pi_{X_j+X_{j'}=0}$ is equal to the projector onto the eigenspace of the target operator $W_{j,j'} = X_j X_{j'}$ with eigenvalue $-1$, which we denote $\Pi_-$. The orthogonal projector onto the eigenspace $+1$ is equal to $\Pi_+ = \Pi_{X_j+X_{j'}=+2} + \Pi_{X_j+X_{j'}=-2}$, and so we identify

$$|\Phi\rangle = e^{-i\pi X_j/2}\Pi_+ |\psi\rangle_{jj'} \otimes |-\rangle_b + \Pi_- |\psi\rangle_{jj'} \otimes |+\rangle_b , \tag{S6}$$

where we have used $e^{-i\pi X_j/2}\Pi_{X_j+X_{j'}=\pm 2} = \mp i\Pi_{X_j+X_{j'}=\pm 2}$. From this expression, we see that if the ancilla is measured in the $X_b$ basis, then an outcome of $+1$ will project the system qubits onto the space with a domain wall present, spanned by $\Pi_-$. The opposite outcome of $+1$ projects the system qubits onto the orthogonal space, with no domain wall present, with an additional single-qubit $X_j$-$\pi$-pulse applied. This extra gate can be explicitly corrected whenever this measurement occurs, although this is not actually necessary to observe time-crystalline order, since the $X_j$ gate does not disturb the key correlations in the system.

If the native gates of the quantum simulator in question are different from the cross-resonance gate, then it may still be possible to measure the domain wall operators using the same principle. Many commonly-used two qubit gates are equivalent to $U_{\mathrm{CR},j,k,\theta}$ when conjugated with single-qubit unitaries. For instance, if one has access to a CPHASE gate $U_{\mathrm{CPHASE},j,k,\theta} = e^{-i\theta(1-Z_j)(1-Z_k)/4}$ (or a CZ gate), then one can apply Hadamard gates to the system qubits $j$, $k$ before applying $U_{\mathrm{CPHASE},j,b,\pi}U_{\mathrm{CPHASE},j',b,\pi}$. Measuring the ancilla qubit in the $X_b$ basis then reveals the presence or absence of a domain wall, as before, and finally Hadamard gates can be applied again to counteract the initial rotations.

Finally, we note that a slightly modified approach to implementing the channel (2) can be constructed that removes the need for projective measurements, which are typically very slow compared to gate times, at the expense of requiring more two-qubit gates. The cross-resonance gates described above are applied to the $(j, j+\hat{e})$ bond using one ancilla $b_e$, and the same for the $(j, j+\hat{n})$ bond using a different ancilla $b_n$ [this is possible given the connectivity of the lattice in Fig. 2(b)]. Then, rather than measuring the two ancillas separately and acting on the central qubit $j$, one can instead implement a three-qubit quantum gate that has the effect of applying a $Z$ gate to the central qubit if both ancilla qubits are in the state $|+\rangle$. This gate is equivalent to a Toffoli gate up to single-qubit rotations, and so can be built up of several two-qubit unitaries [63]. Afterwards, the ancilla qubits can both be reset and prepared in the state $|+\rangle_b$ again, so that they are ready for the next timestep. Overall, this is potentially a much faster process, since the non-unitary processes involved (qubit resets) can be implemented more rapidly than measurements [51].

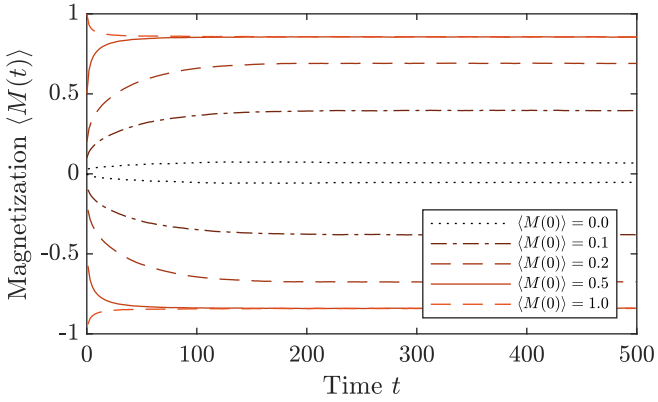


FIG. S2. Expectation of magnetization as a function of time $t$ starting from random $X_j$-basis product states with varying mean magnetization (different shades of red and line type); even and odd times are plotted separately, $L = 20$. The data are averaged over $10^4$ samples. All parameters are as in Fig. 1.

### Initial States and Autocorrelator

Here we provide results of additional numerical simulations that probe the initial-state dependence of the magnetization dynamics, the behaviour of the autocorrelator, and the critical dynamics of the measurement-feedback model.

*Initial state dependence.*—The results shown in the main text (Fig. 1) are for a system that is initialized in a perfectly magnetized state $\rho(0) = |+^{\otimes N}\rangle\langle+^{\otimes N}|$. However, a true time crystal should exhibit such oscillations for generic initial states [2]. In an MBL-DTC, the initial state $\rho(0)$ determines the expectation values of l-bit operators $\tau_j^z$, which evolve according to $\tau_j^z(t+1) = -\tau_j^z(t)$. The amplitude of the oscillations of a particular observable $A$ is then determined by these expectation values $\mathrm{Tr}[\rho(0)\tau_j^z]$ combined with the operator-space overlaps of $A$ with $\tau_j^z$ (compound l-bit operators $\tau_{j_1}^z\tau_{j_2}^z\cdots$ should also be included). For typical initial states with low enough entanglement (e.g. product states), the oscillation amplitude of some appropriately chosen local observable $A$ will indeed be non-zero, and so DTC order can be observed without having to prepare a particular initial state.

In our non-unitary model, there is not an extensive number of emergent conserved quantities; rather the space of stable states has dimension 2. Thus, in the DTC phase (in the thermodynamic limit) it is possible to identify two right eigenoperators of $\mathcal{N}$ — $\rho_{\mathrm{ss}}$ and $\tau$ — with traces 1, 0, and corresponding eigenvalues 1, $-1$, respectively. Without any fine-tuning, all other eigenoperators of $\mathcal{N}$ will have modulus less than 1, so in the late-time limit ($1 \ll t \ll e^{L/\xi}$), the state of the system will be

$\rho(t) = \rho_{\rm ss} + \alpha(-1)^t\tau$, where the coefficient $-1 \leq \alpha \leq 1$ is determined by the initial state. (The coefficient of $\rho_{\rm ss}$ must be unity to ensure the correct trace, and we normalize $\tau$ such that $\mathrm{Tr}[\tau^\dagger\tau] = 1$.) One can then view the extremal density matrices $\rho_\pm \coloneqq \rho_{\rm ss} \pm \tau$ as basins of attraction in the space of possible states [28]. An arbitrary initial density matrix can be split into one part that lies in the basin of $\rho_+$, and another in the basin $\rho_-$; the relative weights of these two parts is what determines $\alpha$. Thus, we expect that our system will display robust oscillations for generic initial states, but the mechanism is somewhat different to the MBL-DTC.

To confirm this expectation, we have calculated the time-dependence of the expectation value of magnetization $M = N^{-1}\sum_j X_j$ for systems that are initialized in random product states — specifically each qubit is in an eigenstate of $X_j$ with eigenvalue $+1$ $(-1)$ with probability $(1 + \langle M(0)\rangle)/2$ ($\langle M(0)\rangle$ is the mean initial magnetization). The results are plotted in Fig. S2. When $\langle M(0)\rangle$ is high enough, most initial states being sampled have a sufficiently large net magnetization to lie entirely within one basin of attraction, so $\alpha = 1$. We see that this is the case when $\langle M(0)\rangle$ is set to 0.5 and 1. As $\langle M(0)\rangle$ it becomes increasingly likely for the initial state of a particular sample to lie within the opposite basin, leading to a decrease of the average value of $\alpha$, and in turn oscillations with smaller amplitude. The width of the distribution of initial magnetization decreases with increasing system size, so we expect that the modulation of $\alpha$ with $\langle M(0)\rangle$ will be less severe with increasing $L$ (we have confirmed this with simulations for different $L$). Note that in our simulations, the Ising symmetry is weakly broken, which means that the fine-tuned point where $\alpha = 0$ and the oscillations vanish is not constrained to occur at zero average initial magnetization.

*Autocorrelator.*—The autocorrelator is defined as $C_t(j, j') \coloneqq \langle X_j(t)X_{j'}(0)\rangle$, where the expectation value is taken with respect to a steady state of the dynamics. In the DTC phase, this steady state consists of an equal-weight combination of positive- and negative-magnetized oscillating states. We prepare this state by initializing the system in the 'paramagnetic' state $|0^{\otimes N}\rangle$ (which has no bias between $+X_j$ and $-X_j$ magnetizations), and evolving for a sufficiently long time such that expectation values of observables become time-independent. We then perform a projective measurement of $X_{j'}$, giving a random outcome $m = \pm 1$, evolve for a further time $t$, and finally compute the expectation value of $X_j$ and multiply it by $m$. We repeat this, stochastically sampling the measurement outcomes $m$ each time, to obtain an estimate of the autocorrelator. The total number of repetitions per data point of our simulation is $10^5$.

Results for two different sets of parameters are shown in Fig. S3, for a system of size $L = 20$. The solid lines correspond to the same parameters as in Fig. 1, which belongs to the DTC phase, while for the dashed lines the rate of unitary gates $p_{\rm unit}$ is set to 0.1, which drives the system into a paramagnetic phase. We see that $C_t(j, j')$ saturates to a non-zero value in the limit of large distance and/or long times in the DTC phase, thus demonstrating the existence of true spatiotemporal order [41]. At odd times (not shown), the sign of this value is reversed, which distinguishes the DTC from the ferromagnetic phase. In the paramagnetic phase, correlations decay rapidly with increasing distance and time.

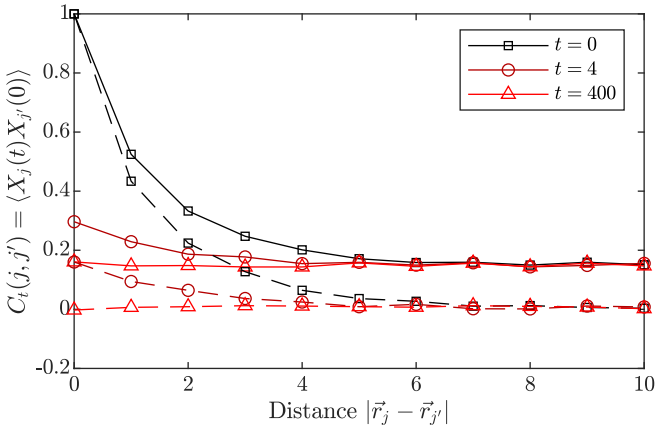


FIG. S3. Behaviour of the autocorrelator $C_t(j, j')$ as a function of the distance between qubits, for different times, on a $L \times L$ square lattice with $L = 20$. The coordinates of the qubits are $j = (0, 0)$, $j' = (x, 0)$, for various $x$. The solid lines are for a system in the DTC phase (same parameters as Fig. 1), while the dashed lines are for a system where $p_{\rm unit}$ is increased to 0.1, putting it in the paramagnetic phase. In the limit of large separation $|\vec{r}_j - \vec{r}_{j'}| \to \infty$, the autocorrelator approaches a non-zero distance-independent value in the DTC phase, indicating the presence of spatiotemporal order. In the paramagnetic phase, the autocorrelator approaches zero as distance and/or time is increased.

## Critical Behaviour

In this section, we discuss the critical behaviour of our model when tuned close to a phase transition. We will focus on the transition between time-crystalline and paramagnetic phases, using the rate of entangling unitary gates $p_{\rm unit}$ as a tuning parameter. In the following, we set $(p_{\rm flip}, p_{\rm NEC}, p_{\rm reset}, p_{\rm ME}) = (0.95, 0.8, 0, 0)$. The dynamics is therefore symmetric under the up-down symmetry $X_j \to -X_j$.

Firstly, we consider the instantaneous properties of the steady states to extract static critical properties. To do so, we initialize the system in an up-down-symmetric state (in particular we choose $|0\rangle^{\otimes N}$), and evolve until a steady state is reached. The magnetization $\langle M\rangle$ (where

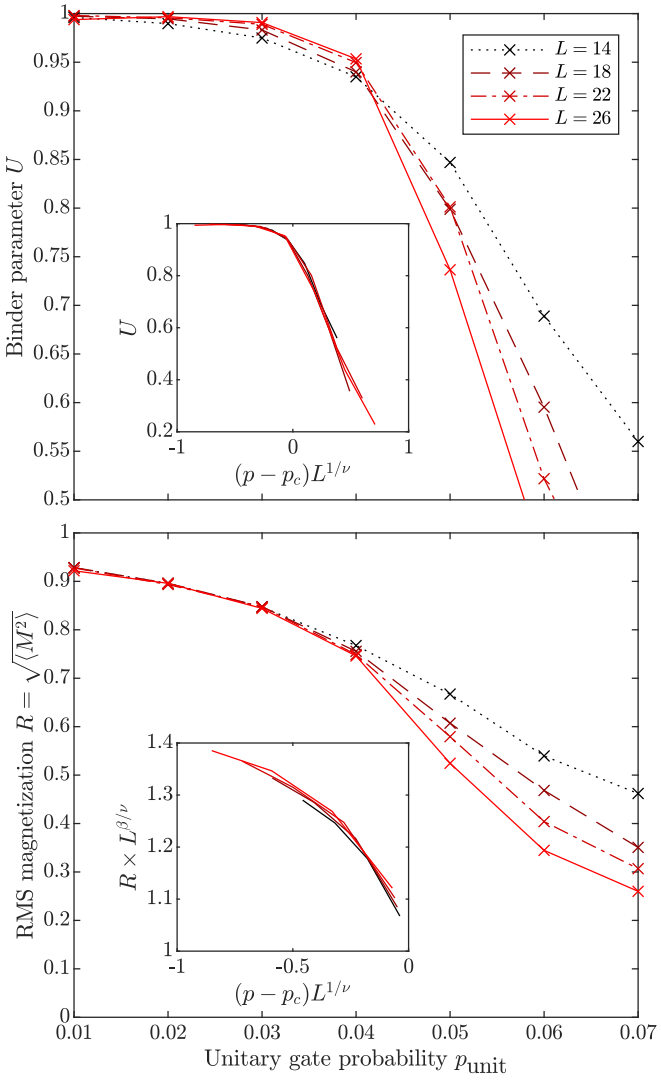


FIG. S4. Critical behaviour of the Binder parameter $U = (3 - \langle M^4 \rangle / \langle M^2 \rangle^2)/2$ (top), where $M = N^{-1} \sum_j X_j$ is the sample magnetization, and the RMS magnetization $R = \sqrt{\langle M^2 \rangle}$ (bottom), using the unitary gate probability $p_{\text{unit}}$ as a tuning parameter. Other parameters are $p_{\text{NEC}} = 0.8$, $p_{\text{flip}} = 0.95$; we do not include resets and measurement errors. We estimate the critical value of the unitary gate probability to be $p_{\text{unit}} = p_c \approx 0.0427$ using the crossing point of the Binder parameter. Insets: Scaling collapse of the data using the 2D Ising critical exponents $\nu = 1$, $\beta = 1/8$.

$M = N^{-1} \sum_j X_j$) must vanish by symmetry, but the even moments $\langle M^2 \rangle$, $\langle M^4 \rangle$ provide information about the symmetry-breaking order. As well as the RMS magnetization $\sqrt{M^2}$, a useful quantity is the Binder parameter $U = (3 - \langle M^4 \rangle / \langle M^2 \rangle^2)/2$ [64], which in classical Ising models approaches 1 in the ordered phase, and 0 in the disordered phase. Finite-size scaling can be used to identify the critical point, where the value of the binder parameter becomes system-size independent. When the location of the critical point is known, it is then possible

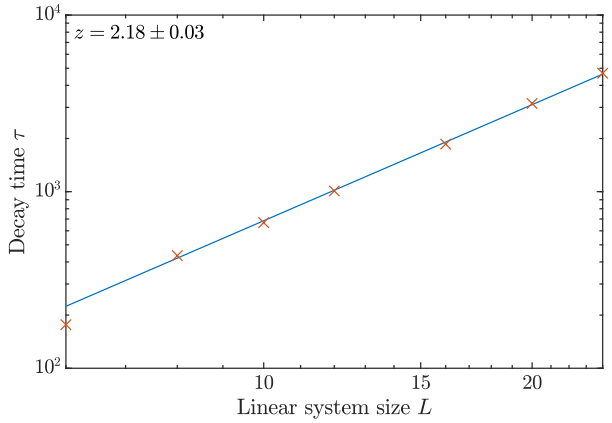


FIG. S5. Dependence of the decay timescale $\tau$ [calculated as in Fig. 1(b)] on the linear system size $L$ under dynamics tuned to the critical point, plotted on a log-log scale. Parameters are as in Fig. S4, with $p_{\text{unit}} = p_c \approx 0.0427$. We fit the data to a power law $\tau \propto L^z$, and find a dynamical critical exponent of $z = 2.18 \pm 0.03$.

to extract critical exponents for the transition.

Our results are shown in Fig. S4. We find a critical unitary gate probability of $p_c \approx 0.0427$. Using this value, we find that the data collapses well using the 2D Ising critical exponent $\nu = 1$. The critical behaviour of the Ising symmetry-breaking order parameter $R = \sqrt{M^2}$ is also shown. Again, we see a good collapse of data using the Ising critical exponent $\beta = 1/8$. This indicates that the transition is in the 2D Ising universality class.

Secondly, we focus on dynamical critical behaviour. In particular, to extract the dynamical critical exponent $z$, we calculate the dependence of the decay timescale of oscillations on the system size $L$, which at criticality should follow $\tau \propto L^z$. This data is shown in Fig. S5, for systems with $p_{\text{unit}}$ tuned to the critical value $p_c \approx 0.0427$. By fitting a power law to the data, we extract a value of $z = 2.18 \pm 0.03$. This is consistent with the best estimates obtained for critical Glauber dynamics of the 2D classical Ising model $z = 2.1667(5)$ [67]. We have confirmed that this value remains unchanged along the phase boundary by performing identical simulations at a critical point where we set $p_{\text{NEC}} = 0.7$, giving a new critical unitary gate probability $p_c' \approx 0.0266$; the power law fit there gives a consistent value of $z = 2.15 \pm 0.03$.

The collection of critical exponents we find (both static and dynamical) are the same as those that would be obtained for classical stochastic dynamics at a phase transition in the 2D Ising universality class. Two comments on this finding are required. Firstly, it is interesting that the critical behaviour of this strongly non-equilibrium model, which does not respect detailed balance, coincides with that of an equilibrium statistical mechanics model. This fits with arguments that (at least for classical systems) the critical exponents for systems with non-conserved order parameter match that would be found in an equilib-

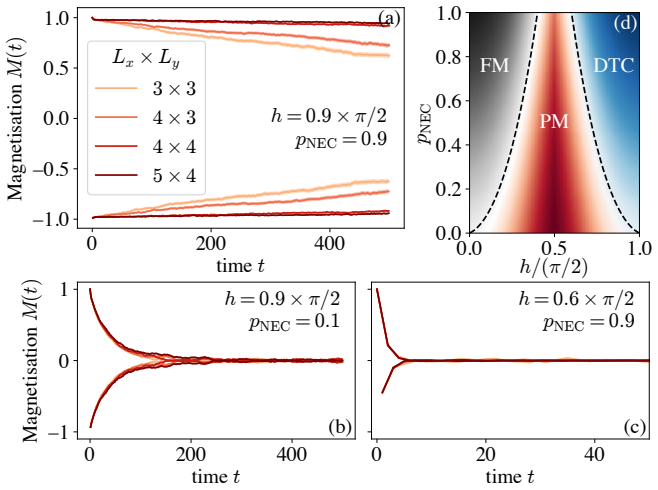


FIG. S6. Numerical results for the model described via Eqs. (S7) and (S8). Panels (a)-(c) show the magnetisation as a function of time for three different values of $(h, p_{\mathrm{NEC}})$ where the different shades denote different system sizes and the two branches denote odd and even stroboscopic times. Panel (d) shows a conjectural phase diagram of the dynamics in the two-parameter space of $h$ and $p_{\mathrm{NEC}}$ with the gray, red, and blue regions corresponding to ferromagnetic, paramagnetic, and time-crystalline spatiotemporal order respectively.

rium model [65]. Note, however, that we expect that certain critical correlators will be sensitive to the lack of microreversibility in our system, as occurs in, e.g. Ref. [42]. Secondly, the appearance of 2D Ising exponents is notably different from what one would expect in the vicinity of a quantum phase transition under unitary dynamics. For instance, in the models discussed in Ref. [66] (under sufficiently generic perturbations), the static critical exponents are those of the 3D Ising universality class, reflecting the effective extra dimension given to the theory under the quantum-classical correspondence. Here, the dynamics is intrinsically non-unitary, and so the state of the system is generically mixed. Thus, the critical theory is closer in nature to a finite-temperature phase transition, rather than being described by a conformal quantum critical point as in [66]. This explains why we find 2D, rather than 3D, Ising critical exponents.

### Numerical simulations beyond Clifford circuits

In this section, we provide proof-of-principle results showing the presence of spatiotemporal order in a setting less restrictive than the Clifford dynamics described until now. The system again comprises of qubits on a rectangular lattice that undergo dynamics described by

$$|\psi(t+1)\rangle = \frac{\mathcal{M}_t U^{(X)} U_t^{(Z)} |\psi(t)\rangle}{||\mathcal{M}_t U^{(X)} U_t^{(Z)} |\psi(t)\rangle||}, \tag{S7}$$

where $U_t^{(Z)} = \exp[\sum_j h_{j,t} Z_j]$ with $h_{j,t} \in [h - \delta h, h + \delta h]$ encodes the noisy, disordered (random in space and time) spin-flips, $U^{(X)} = \sum_{\langle i,j \rangle} J_{ij} X_i X_j$ with $J_{ij} \in [J - \delta J, J + \delta J]$ encodes the interaction between nearest-neighbour qubits on the lattice, and $\mathcal{M}_t$ denotes the measurement and feedback step. The final step, $\mathcal{M}_t = \prod_j \mathcal{M}_{j,t}$, is implemented as

$$\mathcal{M}_{j,t} = \begin{cases} \mathbb{I} & \text{with probability } 1 - p_{\mathrm{NEC}} \\ U_{w_{\hat{n}}, w_{\hat{e}}} \prod_{j,\hat{n}}^{w_{\hat{n}}} \prod_{j,\hat{e}}^{w_{\hat{e}}} & \text{with probability } p_{\mathrm{NEC}} p_{j,t}^{w_{\hat{n}}, w_{\hat{e}}} \end{cases}, \tag{S8}$$

where $p_{\mathrm{NEC}}$ is the probability of measurement and $p_{j,t}^{w_{\hat{n}}, w_{\hat{e}}} = \langle \psi(t) | \prod_{j,\hat{n}}^{w_{\hat{n}}} \prod_{j,\hat{e}}^{w_{\hat{e}}} |\psi(t)\rangle$ is the Born rule probability. We fix $J = 1$ and $\delta J = 0.2 = \delta h$ and study the problem in a two-dimensional parameter space spanned by $h$ and $p_{\mathrm{NEC}}$. Loosely speaking, $h = 0$ and $h = \pi/2$ can be considered analogous to the $p_{\mathrm{flip}} = 0$ and $p_{\mathrm{flip}} = 1$ limits of the Clifford circuit discussed in the main text.

Within this setting, let us now turn towards the results. For simplicity we start from a fully polarised state $|\psi(0)\rangle = |+^{\otimes N}\rangle$ and track the magnetisation $M(t) = N^{-1} \sum_i \langle X_i(t) \rangle$. We expect a robust phase with a time-crystalline spatiotemporal order in the vicinity of $h \sim \pi/2$ and $p_{\mathrm{NEC}} \lesssim 1$. This is indeed bourne out in Fig. S6(a) where the lifetime of the time-crystalline order clearly increases with increasing system size for $h = 0.9 \times \pi/2$ and $p_{\mathrm{NEC}} = 0.9$. On decreasing $p_{\mathrm{NEC}}$, we expect that below a threshold value the corrective feedback becomes weak enough that the inherently noisy and hence thermalising unitary part of the dynamics in Eq. (S7) melts the spatiotemporal order. This is indeed what we see in Fig. S6(b) for $p_{\mathrm{NEC}} = 0.1$. The spatiotemporal order can also be destroyed by tuning $h$ well away from $\pi/2$ such that the spin-flips due to $U_t^{(Z)}$ are effectively weak enough to not induce the temporal order [see Fig. S6(c)]. By analogous considerations in the vicinity of $h \sim 0$, we expect the same phenomenology but for a phase with non-trivial spatial order but no non-trivial temporal order. We do indeed find such a measurement-feedback stabilised ferromagnetic phase but do not show the results for brevity. All of the above can be summarised via the schematic phase diagram shown in Fig. S6(d).